Hindawi
International Journal of Polymer Science
Volume 2022, Article ID 9254833, 12 pages
https://doi.org/10.1155/2022/9254833

Research Article

Residual Strain Monitoring and Dynamic Characteristics of Hybrid Hollow Square Tube with Metal–FRP–Metal Sandwich Walls

Zhao Li,[1] **Mingyao Liu**,[1] **Jintao Wang**,[1] **and Wei Ke**[2]

[1]*School of Mechanical and Electronic Engineering, Wuhan University of Technology, Wuhan, Hubei 430070, China*
[2]*State Key Laboratory of New Textile Materials and Advanced Processing Technologies, School of Textile Science and Engineering, Wuhan Textile University, Wuhan, Hubei 430200, China*

Correspondence should be addressed to Mingyao Liu; myliu@whut.edu.cn and Wei Ke; wke@wtu.edu.cn

Received 10 July 2022; Revised 19 September 2022; Accepted 18 October 2022; Published 28 October 2022

Academic Editor: Yasir Nawab

In order to design and fabricate a novel hollow square tube (HST) for ram structure in machine tools, the hybrid HST with sandwich walls based on steel skins and unidirectional carbon fiber-reinforced polymer (CFRP) composite core is proposed. A detailed co-cured fabrication method with embedded fiber Bragg grating (FBG) sensors for residual strains/stresses determination in a hybrid metal–composite structure is presented. Results reveal that the hybrid HST has undergone complex residual strain history, and the strain rate is about 10 times the cooling rate. The tensile strains in the dwell stage transform into compressive strains in the cooling stage due to the mismatch of the coefficients of thermal expansion of the steel plates and the CFRP composite. A comparison of the residual strains in the cooling phase obtained by FBG sensors with those obtained by theoretical calculation is carried out. Furthermore, the dynamic characteristics of the hybrid HST and the steel HST are tested. The results showed that the damping of the hybrid HST is 586% higher than that of the steel HST, while the hybrid HST has a lower first natural frequency (4.6% reduction) and mass (15.9% weight reduction). The influence of co-cure temperature and cooling rate on the size and state of the residual strains is analyzed, which might be helpful to guide the manufacturing of sandwich structures in machine tools. This novel hybrid HST may be used for online health monitoring and safety evaluation to build intelligent machine tools structures.

1. Introduction

Hollow square tubes (HSTs) are common engineering components with an efficient shape due to their high inherent bending stiffness and torsional stiffness, and have gained widespread use in navigation, vehicle, and bridge structures. Ram structure moves along the guide way in the headstock to provide support and workspace for rotating spindle with tools typically in a heavy floor-type milling and boring machine tool. HSTs with sandwich walls have been used as a potential application of ram structure due to their thin faces and various cores, which have been considered as structures of lightweight, superior strength, and stiffness [1, 2]. To date, the ram structure has the topology of an HST with monolithic metal walls and internal stiffeners, which support the monolithic metal walls for enhancing the local bending stiffness. An alternative topology is to use sandwich walls instead of stiffeners, giving lower mass with comparable stiffness. Moreover, the open architecture provided by sandwich walls can integrate sensors or actuators into the hybrid structure [3].

Sandwich structures are formed by two thin, stiff, strong faces, such as metal or fiber-reinforced polymer (FRP) composites, and a lightweight core material, such as foam materials, honeycomb, FRP composites, and balsa. For ram structure, both inside and outside surfaces are connected and moved with metallic spindle and headstock, respectively. As a consequence, the faces should be metals for more reliable connection and machining accuracy compared with FRP composites. Besides, compared with conventional materials, FRP composites

display a wide variety of advantages, such as lightweight, high specific strength and stiffness, good damping capacity, and tailorable ability [4]. Considering that the ram bear vibration is the main source of resonance, metal–FRP–metal sandwich walls can increase its fundamental natural frequency and decrease the vibration-induced. However, most of the research about metal–composite sandwich structures mainly focuses on sandwich beams and flat panels. To the authors' knowledge, only a few studies are reported for the circular tube with metal–FRP walls [5–7], and no study is reported for HST with metal–FRP–metal sandwich walls due to difficult fabrication.

To deal with this problem, the hybrid HST has been divided into FRP layers and three metal parts and connected by co-cured bonding, whose adhesive is the excess resin extracted from composite prepreg during cure and consolidation processes. However, large thermal residual strains/stresses are generated during the co-curing process due to differences in elastic properties and coefficients of thermal expansion (CTE) of the FRP and metal layers. The thermal residual strains/stresses during fabrication greatly cause several defects in hybrid structures, such as transverse cracking and delamination, decrease in the fatigue performance and dimensional accuracy, reduce in the structure's strength and modulus, and impact on the natural frequencies and flexural stiffness [8]. Since the FRP layers and interfaces are a typical weak point of hybrid metal–composite structures, formation mechanism [9], influencing factors [10], analytical approaches [11], and measurement methods [12–17] of the thermal residual strains/stresses in FRP layers are studied in the literature. The measurement methods can be divided into three categories: non-destructive, semi-destructive, and destructive [18]. As a non-destructive measurement method, the fiber Bragg grating (FBG) sensor is used to monitor residual strain development during cure processing because it is small in diameter, precise, stable, easy integration, and anti-interference [19]. Several studies have been conducted to use FBG sensors for the online health monitoring and safety evaluation of FRP composite structures [20–24]. However, research about metal–composite sandwich structures with embedded FBG sensors is rare [25, 26]. To the authors' knowledge, no study is reported for metal–FRP–metal sandwich walls for HST with embedded FBG sensors.

This study presents a novel hybrid HST with sandwich walls based on steel skins and a unidirectional carbon fiber-reinforced polymer (CFRP) composite core and a detailed fabrication method with embedded FBG sensors. The embedded FBG sensors are combined to monitor the temperature and strain history in real time. Dynamic characteristics of the hybrid HST and the steel HST are tested.

2. Experimental Procedure

2.1. Theory of FBG Sensor. The FBG is composed of the periodic distribution of the refractive index, which is made by ultraviolet exposure in the optical fiber core. When an incident broadband light passes through an FBG, a narrow-band light with a particular wavelength, which is called Bragg wavelength, is reflected. The Bragg wavelength, λ_B, satisfies the Bragg scattering condition. It is expressed by the following equation [27]:

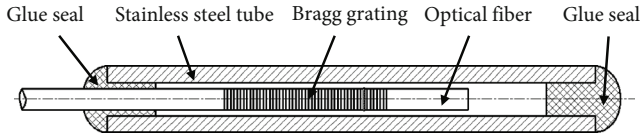

Figure 1: Encapsulated FBG for temperature measurement.

$$\lambda_B = 2 \cdot n_{\text{eff}} \cdot \Lambda. \quad (1)$$

The value of the Bragg wavelength depends on the effective refractive index of the fiber core, n_{eff}, and the grating period, Λ. However, when the FBG is subjected to axial strain ε or temperature changes ΔT, both the grating period and the effective refractive index change, and then result in the Bragg wavelength shift, $\Delta\lambda_B$. The Bragg wavelength variation, which is sensitive to strain and temperature, can simultaneously be expressed as:

$$\Delta\lambda_B = \lambda_B(1 - P_e)\varepsilon + \lambda_B(\alpha_f - \xi)\Delta T = K_\varepsilon \varepsilon + K_T \Delta T, \quad (2)$$

where P_e, α_f, and ξ are the effective photoelastic coefficients, the thermal expansion coefficients, and the thermo-optic coefficients, respectively, and K_ε and K_T are the strain sensitivity constants and the temperature sensitivity constants, respectively. The strain and temperature sensitivity constants of FBG sensors depend on the type of fibers. As P_e has a typical value of 0.22 for fused silica [26], K_ε is 1.2 pm/$\mu\varepsilon$ in this study without calibration for an FBG of a central wavelength of 1547 nm. However, K_T requires a calibration procedure because of the non-linear thermal-optic behavior of FBGs in the range of the curing temperatures. The detailed calibration procedure can be seen in the next section.

According to Equation (2), it can be found that the changes of FBG wavelength are proportional to axial strain and temperature. As a consequence, a single FBG cannot avoid strain–temperature cross-sensitivity, as both strain and temperature induce a Bragg wavelength shift. Several techniques to achieve such discrimination are available in the literature [28]. In this study, two separate FBG sensors are embedded into a structure to avoid FBG cross-sensitivity. The FBG temperature sensor (FBGTS) is a 10 mm long FBG encapsulated in a stainless steel tube, as shown in Figure 1. Considering a normal optical fiber with an outer diameter of 0.125 mm, the inner and outer diameters of the stainless steel tube are 0.2 and 0.4 mm, respectively, as small as possible to avoid affecting hybrid structural integrity. As a consequence, the FBGTS only has relationship with the temperature change theoretically. Therefore, Equation (2) can be simplified as:

$$\Delta\lambda_{B1} = K_{T1}\Delta T. \quad (3)$$

The FBG strain sensor (FBGSS) is a bare FBG with no treatment and is affected by axial strain and temperature. In this study, the FBGTS is placed near the FBGSS for the same temperature changes. Then, the axial strain can be

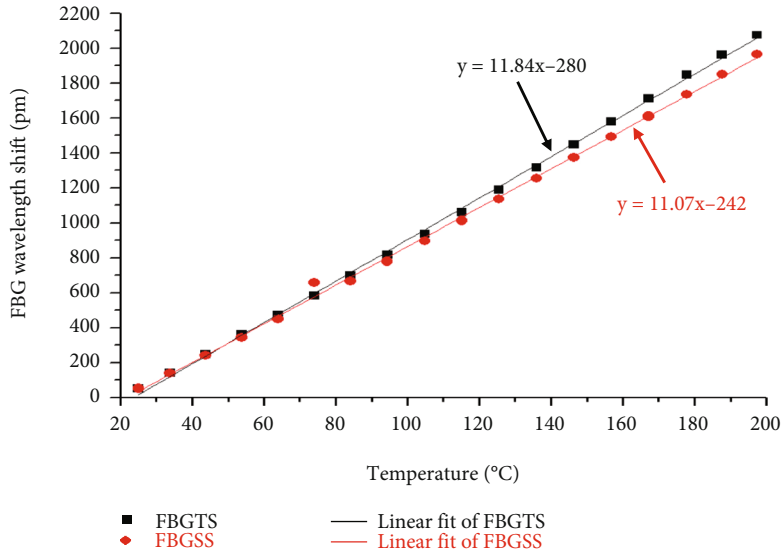

Figure 2: Temperature sensitivity of the FBGTS and FBGSS.

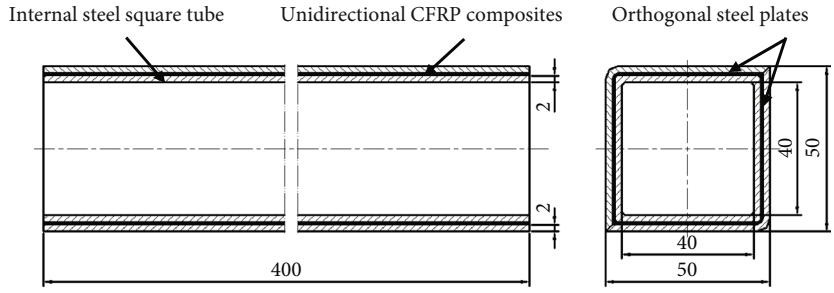

Figure 3: Dimensions of the hybrid HST with sandwich walls.

obtained from the measured wavelength shift by combining Equation (2) with Equation (3).

$$\varepsilon = \frac{\Delta\lambda_B}{K_\varepsilon} - \frac{(\Delta\lambda_{B1}K_T)}{(K_{T1}K_\varepsilon)}. \quad (4)$$

2.2. Temperature Calibration. Two FBGs (FBGTS and FBGSS) and a standard K-type thermocouple are fixed on an aluminum plate with a thermally conductive adhesive in an oven. It is ensured that the FBGs are in strain-free condition, so they responded to temperature change only. The Bragg wavelength shifts of FBGs are monitored by an FBG interrogator with a minimum resolution of 1 pm and a maximum sampling frequency of 4 kHz. For the FBGTS and the FBGSS, the initial central wavelengths are 1546.860 and 1546.936 nm, respectively, by the FBG interrogator. It must be confirmed the reliability of the encapsulated FBGTS before the calibration procedure. When the FBGTS is subjected to axial load at room temperature, no obvious wavelength shift is observed, so the FBGTS is considered to be in strain-free condition. Both signal wires of FBGs and thermocouple are through the sealing strip of the oven door and connected to the FBG interrogator and the thermocouple temperature indicator. Results of the Bragg wavelength shifts are recorded by a computer.

The Bragg wavelength shifts versus temperature for both the FBGTS and FBGSS are shown in Figure 2. From the linear fitting results, K_T of the FBGTS is 11.84 pm/°C (K_{T1} = 11.84 pm/°C) with a fitting linear correlation coefficient of 99.91%. For the FBGSS, K_T is 11.07 pm/°C with a fitting linear correlation coefficient of 99.82%.

2.3. Fabrication Method of the Hybrid HST with Embedded FBG Sensors. The hybrid HST with sandwich walls based on steel skins and a unidirectional CFRP composite core is designed and fabricated in this section. As shown in Figure 3, the hybrid HST is composed of an internal steel square tube, a square layer of unidirectional CFRP composite, and two orthogonal steel plates. The hybrid HST with dimensions of $50 \times 50 \times 400\,mm^3$ is a fifth of the size of the real ram structure with dimensions of $250 \times 250 \times 2000\,mm^3$. The unidirectional CFRP composite core in this study consists of 10 layers of USN 10000/T300 prepreg from Weihai Guangwei Composites Company with dimensions of $460 \times 1000 \times 0.1\,mm^3$. The material of the steel square tube is American Iron and Steel Institute (AISI) 1045 based on the AISI grade system. The chemical composition of AISI 1045 is listed in Table 1 according to the ASTM A 29/A 29M-05 [29]. Material properties of the unidirectional CFRP composite and the steel square tube are listed in Table 2. The

Table 1: Chemical composition of AISI 1045.

Steel grade	Chemical composition (%)			
	C	Mn	P	S
AISI 1045	0.43–0.50	0.60–0.90	≤0.040	≤0.050

Table 2: Material properties of the unidirectional CFRP composite and the steel square tube.

Material properties	USN 10000/T300 prepreg	AISI 1045
Longitudinal modulus, E_1 (GPa)	137	200
Transverse modulus, E_2 (GPa)	9	200
Shear modulus, G_{12} (GPa)	3.78	80
Major Poisson's ratio, ν_{12}	0.28	0.29
Longitudinal CTE, α_1 (10^{-6}/°C)	−0.5	11
Transverse CTE, α_2 (10^{-6}/°C)	27	11
Density (g/cm^3)	1.76	7.85

detailed fabrication processes are shown in Figure 4. Finally, the clamped hybrid HST is shown in Figure 4(g).

(a) The internal steel square tube is cut from a continuous seamless steel tube with dimensions of $44 \times 44 \times 400\,\text{mm}^3$, while two orthogonal steel plates are bent and machined from steel plates, respectively, which are assembled exactly into an external steel square tube. After manufacturing the internal steel square tube and orthogonal steel plates, metal surfaces need to be roughened with wire wheels to increase the interfacial adhesive strength between the metal plate and the prepreg. Finally, metal surfaces are degreased and cleaned with acetone [30, 31].

(b) Wrapping 5 unidirectional carbon fiber epoxy composite prepreg layers on the internal steel square tube by hand layup and the fiber direction of the unidirectional prepreg is aligned with the axis of the internal steel square tube to obtain high stiffness in the axial direction.

(c) Placing the FBGSS in the middle of the face of the HST, the FBGTS placed nearby can be used for temperature compensation. The two optical fibers are protected by a Teflon tube in the egress location.

(d) Wrapping 5 unidirectional carbon fiber epoxy composite prepreg layers as same as step 2 to make the total prepreg layers 1 mm thick.

(e) Covering the wrapped internal steel square tube and sensors with the two orthogonal steel plates, which compose an external steel square tube.

(f) Clamping the hybrid HST with orthogonal clamps and screws at both ends to ensure enough contact between the steel–CFRP–steel sandwich walls for effective co-cure bonding.

2.4. Experimental Setup for the Co-Curing Process. The experimental setup for the hybrid HST with sandwich walls is shown in Figure 5. The clamped hybrid HST is put in the high-low temperature oven. A standard K-type thermocouple is fixed on the surface of the hybrid HST with thermally conductive adhesive. Both signal wires of FBGs and thermocouple are through a specially reserved sealing hole in the oven wall and connected to the FBG interrogator and the thermocouple temperature indicator. The computer is used to record the Bragg wavelength shifts of FBGs by the cable connected to the FBG interrogator.

The co-cure bonding of the HST with sandwich walls is manufactured under the manufacturer's recommended cure cycle (MRCC), as shown in Figure 6. The process is a typical curing cycle for thin CFRP/epoxy composite and is characterized by a heat-up ramp and dwell stages. The temperature is enhanced to the cure temperature (120°C) in 1.5 hours and held for 1.5 hours. Finally, the clamped hybrid HST is cooled to room temperature. During those stages, the adhesive bonding between the unidirectional CFRP composite and internal/external steel square tube is realized by the resin extracted from the prepreg layers. During the cooling process of the co-curing, thermal residual strains/stresses appear due to the different CTE between the steel and the composite.

2.5. Evaluation of Thermal Residual Strains Based on the Classical Lamination Theory. Classical lamination theory (CLT) is applied to predict the laminate properties of orthotropic continuous fiber laminated composites. The stiffness and transformation matrices for predicting the engineering constants of the CFRP layers are expressed as follows [32].

The stiffness matrix $[Q]$ and transformation matrix $[T]$ are:

$$[Q] = \begin{bmatrix} \dfrac{E_1}{1-\nu_{12}\nu_{21}} & \dfrac{\nu_{12}E_2}{1-\nu_{12}\nu_{21}} & 0 \\ \dfrac{\nu_{21}E_1}{1-\nu_{12}\nu_{21}} & \dfrac{E_2}{1-\nu_{12}\nu_{21}} & 0 \\ 0 & 0 & G_{12} \end{bmatrix}, \tag{5}$$

$$[T] = \begin{bmatrix} \cos^2\theta & \sin^2\theta & 2\sin\theta\cos\theta \\ \sin^2\theta & \cos^2\theta & -2\sin\theta\cos\theta \\ -\sin\theta\cos\theta & \sin\theta\cos\theta & \cos^2\theta - \sin^2\theta \end{bmatrix}. \tag{6}$$

The stiffness for angled lamina is:

$$\left[\bar{Q}\right] = [T]^{-1}[Q]\begin{bmatrix} 1 & 0 & 0 \\ 0 & 1 & 0 \\ 0 & 0 & 2 \end{bmatrix}[T], \tag{7}$$

where E_1, E_2, G_{12}, ν_{12}, ν_{21}, and θ represent longitudinal Young's modulus, transverse Young's modulus, shear modulus, major Poisson's ratio, minor Poisson's ratio, and lamina orientation angle, respectively.

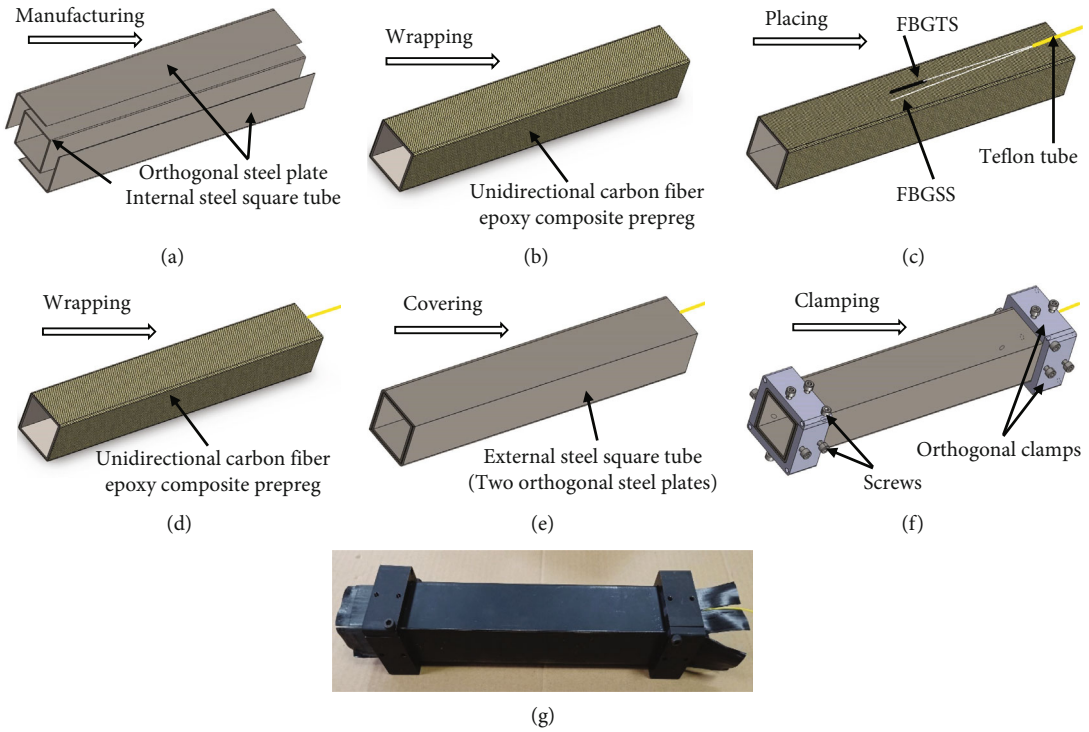

Figure 4: Fabrication processes for the hybrid HST with sandwich walls: (a) manufacturing, (b) wrapping, (c) placing, (d) wrapping, (e) covering, (f) clamping, and (g) photograph of the clamped hybrid HST.

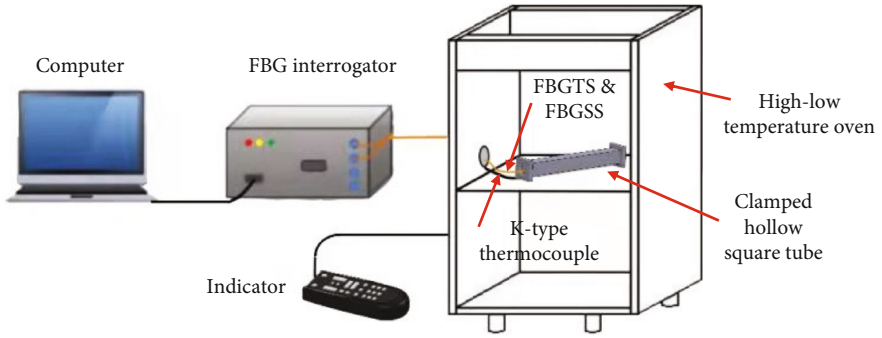

Figure 5: Experimental setup for the hybrid HST with sandwich walls.

The extensional stiffness matrix $[A]$, strain-curvature coupling stiffness matrix $[B]$, and bending stiffness matrix $[D]$ for laminate are given by:

$$[A] = \sum_{k=1}^{N} \left(\bar{Q}_{ij}\right)_k (z_k - z_{k-1}) \sum_{k=1}^{N} \left(\bar{Q}_{ij}\right)_k t_k, \tag{8}$$

$$[B] = \frac{1}{2} \sum_{k=1}^{N} \left(\bar{C}_{ij}\right)_k \left(z_k{}^2 - z_{k-1}{}^2\right) \sum_{k=1}^{N} \left(\bar{C}_{ij}\right)_k t_k \bar{z}_k, \tag{9}$$

$$[D] = \frac{1}{3} \sum_{k=1}^{N} \left(\bar{C}_{ij}\right)_k \left(z_k{}^3 - z_{k-1}{}^3\right) = \sum_{k=1}^{N} \left(\bar{C}_{ij}\right)_k \left(t_k z_k{}^{-2} + \frac{t_k{}^3}{12}\right), \tag{10}$$

where z_k and t_k represent the vertical position of the kth lamina from the mid-plane and thickness of the kth lamina, respectively.

For symmetric laminate, the effective longitudinal Young's modulus of the laminate E_x, the effective transverse Young's modulus of the laminate E_y, the effective laminate in-plane shear modulus G_{xy}, and the effective laminate longitudinal Poisson's ratio ν_{xy} are defined as:

$$E_x = \frac{\sigma_x}{\varepsilon_x^0} = \frac{A_{11}A_{22} - A_{12}{}^2}{tA_{22}}, \tag{11}$$

$$E_y = \frac{\sigma_y}{\varepsilon_y^0} = \frac{A_{11}A_{22} - A_{12}{}^2}{tA_{11}}, \tag{12}$$

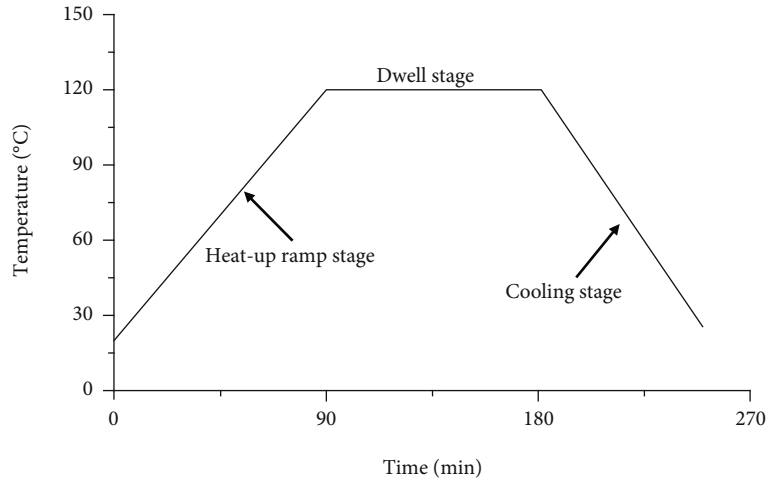

Figure 6: Cure cycle of USN 10000/T300 prepreg from manufacturer.

$$G_{xy} = \frac{\tau_{xy}}{\Upsilon^0_{xy}} = \frac{A_{66}}{t}, \tag{13}$$

$$\nu_{xy} = \frac{A_{12}}{A_{22}}, \tag{14}$$

$$\nu_{yx} = \frac{A_{12}}{A_{11}}, \tag{15}$$

where t represents the thickness of the laminate.

The analytical model considers residual strains produced only during the cooling phase stage, based on the following assumptions [33]: (1) the CFRP layers are plane stresses; (2) each lamina has a unique deformation without stress relaxation; (3) the behavior of each component material is elastic during the cooling process. According to the force equilibrium equation from the mechanics of materials, residual strains in the hybrid HST can be described as:

$$A_s E_s [\varepsilon_s] + A_c [C][\varepsilon_c] = 0, \tag{16}$$

where $[C] = \begin{bmatrix} \frac{E_x}{1-\nu_{xy}\nu_{yx}} & \frac{\nu_{xy}E_y}{1-\nu_{xy}\nu_{yx}} \\ \frac{\nu_{yx}E_x}{1-\nu_{xy}\nu_{yx}} & \frac{E_y}{1-\nu_{xy}\nu_{yx}} \end{bmatrix}$, $[\varepsilon_s] = \begin{bmatrix} \varepsilon_s \\ \varepsilon_s \end{bmatrix}$ and $[\varepsilon_c] = \begin{bmatrix} \varepsilon_{c1} \\ \varepsilon_{c2} \end{bmatrix}$.

Here, A_s and A_c represent the cross-sectional areas of steel and CFRP layers, respectively. E_s and $[C]$ represent Young's modulus of steel and the stiffness matrix of CFRP layers, respectively. ε_s, ε_{c1}, and ε_{c2} represent the strains of the steel, and CFRP layer in the axial and transverse directions, respectively.

Based on the unique deformation, the total strains of the two materials, which are composed of thermal residual strain and thermal strain, can be described as:

$$[\varepsilon_s] + [\alpha_s]\Delta T = [\varepsilon_c] + [\alpha_c]\Delta T, \tag{17}$$

where $[\alpha_s] = \begin{bmatrix} \alpha_s \\ \alpha_s \end{bmatrix}$ and $[\alpha_c] = \begin{bmatrix} \alpha_1 \cos^2\theta + \alpha_2 \sin^2\theta \\ \alpha_1 \sin^2\theta + \alpha_2 \cos^2\theta \end{bmatrix}$.

Here, α_s, α_1, and α_2 denote the CTEs of steel, and CFRP layers in the axial and transverse directions, respectively. ΔT denotes the temperature difference at different phases. Then, from Equations (16) and (17), the thermal residual strain in the CFRP layers can be expressed by:

$$[\varepsilon_c] = [A]^{-1}[B]\Delta T, \tag{18}$$

where $[A] = \left[1 + \frac{E_x A_c}{E_s A_s(1} - \nu_{xy}\nu_{yx}\right) \frac{V_{xy}E_y A_c}{E_s A_s} (1 - \nu_{xy}\nu_{yx}) \frac{V_{xy}E_x A_c}{E_s A_s} (1 - \nu_{xy}\nu_{yx}) 1 + \frac{E_y A_c}{E_s A_s(1-\nu_{xy}\nu_{yx})}]$ and $[B] = [\alpha_s] - [\alpha_c]$.

2.6. Experimental Setup of Modal Testing. Modal testing is performed to study the dynamic characteristics of HST with both sandwich and steel walls under vibrational excitation. According to the experimental equipment as shown in Figure 7, the HST with sandwich walls is suspended to simulate the free–free boundary conditions. For comparison, the same experiment is done for HST with steel walls. An impact hammer is used to excite vibrations of the HST, and the force history of the hammer impact is recorded by the force transducer connected with the hammer. With an accelerometer bonded on the surface, the acceleration response of the HST is detected in a similar way. Then, the excitation and response signals are collected and processed by the LMS analysis system developed by Siemens company. Based on the obtained frequency response function (FRF), the modal parameters including natural frequencies, damping ratio, and modal shapes can be analyzed by the modal analysis module. In order to obtain relatively accurate results, HSTs are measured with 7 excitation points along their length, and each excitation point is applied 3 times to obtain the average FRF.

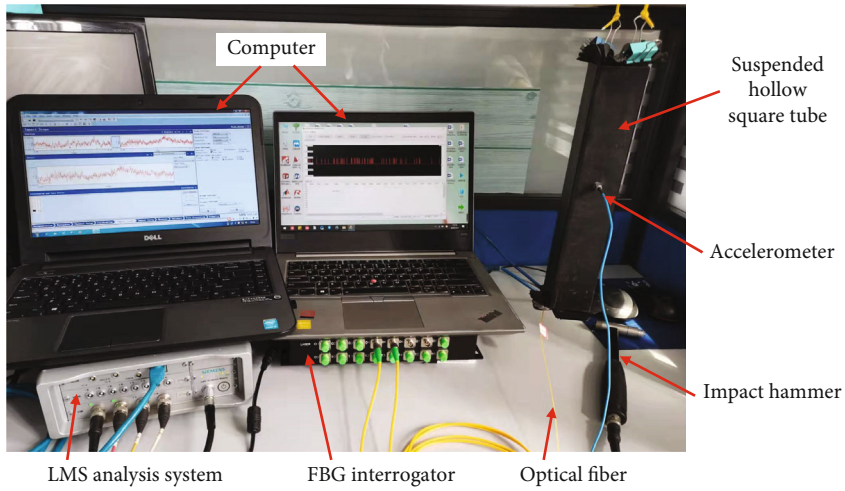

Figure 7: Experimental setup of modal testing.

3. Measurement Results and Discussion

3.1. Temperature History by the FBGTS. The availability of the data obtained from embedded FBG sensors must first be confirmed by observing whether the spectra of embedded FBGTS and FBGSS are distorted by the computer. There is no evident distortion from all the spectra before and after the fabrication process. Simultaneous measurements of temperatures and strains during the co-cure bonding process are performed by the FBG sensors in real time.

The temperature history during the co-cure bonding process by the FBGTS and the thermocouple is presented in Figure 8. It can be observed that the tendency of the temperature measured by the FBGTS has good agreement with the thermocouple. The temperature values are about 1°C lower than that of the thermocouple in the dwell stage. It reflects a temperature gradient on the surface and inside. The temperature gradient decreases in the cooling stage. Therefore, this FBGTS can be used to monitor the temperature process of the hybrid HST and to provide internal temperature for the FBGSS.

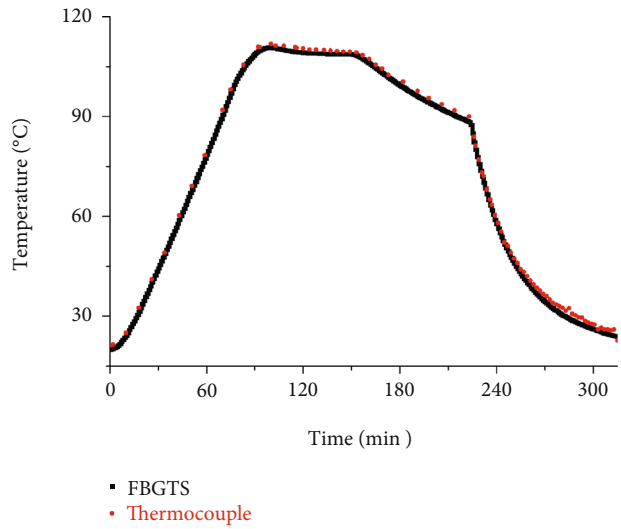

Figure 8: The temperature history during the co-cure bonding process.

3.2. Thermal Residual Strain History by the FBGSS. The plot of temperature and strain history during the co-cure bonding process is given in Figure 9. To better analyze these curves, the co-cure bonding process is divided into 5 phases, as labeled at the top of the curves. Thermal residual strain at the end of each phase is shown in Figure 9, and Table 3 reports the comparison of the residual strains in the cooling phase obtained by the FBGSS and theoretical calculation.

The first phase corresponded to the rise of temperature from 20°C to 70°C at a heating rate of 1.0°C/minutes. The strain curves are almost flat at about zero. Pressure is applied by orthogonal clamps and screws to ensure enough contact between the steel plates and CFRP prepreg layers for effective heat transfer. At this moment, the epoxy resin of CFRP layers is still in a liquid state, which means all the components are free from each other. Although the FBGSS mainly has undergone transverse pressure, the strain response is difficult to interpret in this phase.

The second phase corresponded to the rise in temperature from 70°C to 110°C at a heating rate of 0.9°C/minutes. As the heating rate setting in the heat-up ramp stage is the same, the heating rate is faster in the first phase than that in the second phase mainly because of the heat from the drastic exothermal reaction of the epoxy resin. At the start of this phase, the increasing viscosity during the transformation of the epoxy resin from the liquid into a rubbery state leads to an increasing interaction between the steel plates and CFRP layers. With the gelation of the resin, the resin has not sufficiently reticulated for effective load transfer. The strain curve increase is mostly caused by the huge thermal expansion of the steel plates and CFRP prepreg layers as well as the frictional effect, which is transferred to the FBGSS.

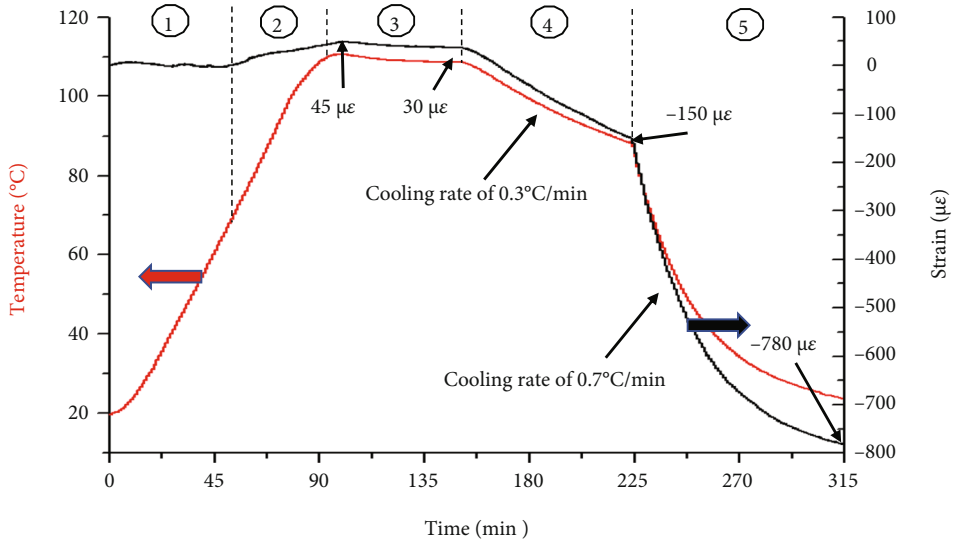

Figure 9: The temperature and strain history during the co-cure bonding process.

Table 3: Comparison of the residual strains in the cooling phase obtained by the FBGSS and theoretical calculation (Equation (18)

Cooling phase (°C)	By the FBGSS ($\mu\varepsilon$)	By theoretical calculation ($\mu\varepsilon$)	Relative difference (%)
110 ⟶ 108	15 (+45 ⟶ +30)	17.8	18.6
108 ⟶ 88	180 (+30 ⟶ −150)	178.6	−0.8
88 ⟶ 23	630 (−150 ⟶ −780)	580.6	−7.8

Table 4: Comparison of the longitudinal residual strains of the fiber layers.

Material combination	Stacking sequence	Curing processes	Residual strains ($\mu\varepsilon$)
Steel/UD-CFRP[a]	$[St/0_5/St]$	MRCC	−810
	$[0_3/St/0_6]_S$	MRCC	−800 [9]
	[0/90/St/0/90]	MRCC	−556 [18]
	$[St/0_4/St/0_2]_S$	MRCC	−786 [15]
	$[St/0_4/St/0_2]_S$	Modified MRCC	−682 [15]
	$[0_{10}/St]$	MRCC	−478 [16]
Aluminum alloy/UD-CFRP[a]	$[Al/0_4/Al]$	MRCC	−922 [17]
	$[Al/0_4/Al]$	CFRP clamped	−734 [17]
Aluminum alloy/UD-GFRP[b]	$[Al/0_2/Al/0_2/Al]$	MRCC	−732 [26]
Titanium alloy/UD-CFRP[a]	$[0_7/Ti/0_7/Ti/0_7/Ti]$	MRCC	−550 [10]

[a]Unidirectional carbon fiber-reinforced polymer prepregs.
[b]Unidirectional glass fiber-reinforced polymer prepregs.

The third phase corresponded to the stable temperature at about 110°C with a slight decrease to 108°C at the end of this phase. In this stage of gelation and vitrification, we started measuring tensile strains caused by the exothermal reaction, compressive strains caused by chemical contraction, and tensile strains caused by the mismatch of the CTE of the steel plates and CFRP layers by FBGSS. Although the maximal residual tensile strain is 45 $\mu\varepsilon$, it can be observed that the residual tensile strain is 30 $\mu\varepsilon$ at the end of this phase. From Table 3, it is observed that the residual strain obtained by theoretical calculation is greater, and the relative difference is +18.6%, because the theoretical calculation does not take into account the exothermal reaction and the chemical contraction. At approximately 60 minute isothermal dwell, we assume that the co-cure bonding is achieved.

The fourth phase corresponded to the fall of temperature from 108°C to 88°C at a cooling rate of 0.3°C/minutes when the high-low temperature oven is turned off. At the start of this phase, the strain curves decline followed by the temperature curves mainly because the gelation and vitrification are completely finished. Then, the tensile strains transform into compressive strains due to the mismatch of the CTE. Because the CTE of the steel plates is much more than the CTE of the CFRP composite as shown in Table 2, the compressive strains are generated during the cooling down of temperature. It can be observed that the residual

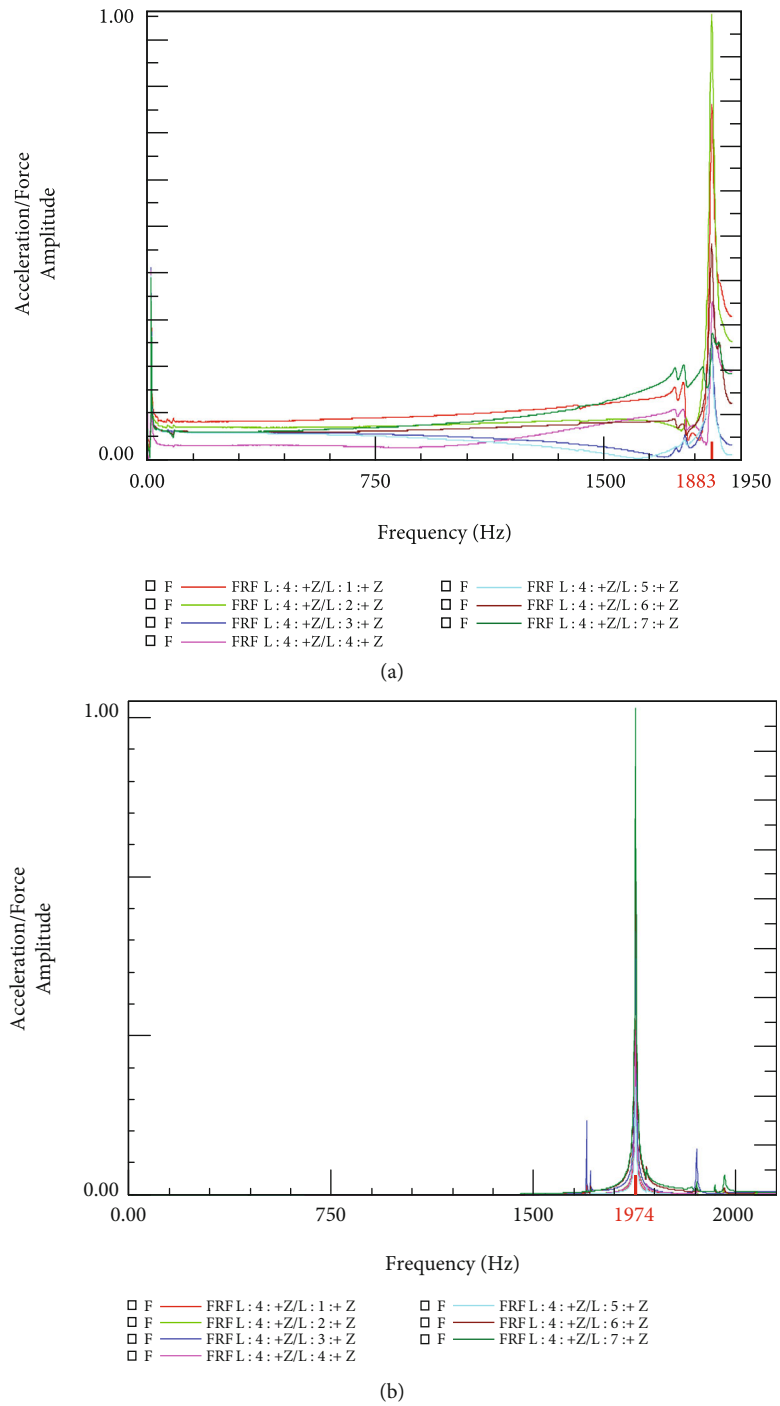

Figure 10: Acceleration FRFs of 7 excitation points for the HSTs: (a) steel–CFRP–steel sandwich walls and (b) steel walls.

compressive strain is 150 $\mu\varepsilon$ at the end of this phase. The residual strain obtained by theoretical calculation is almost identical to that obtained by the FBGSS, with −0.8% of the relative difference, as listed in Table 3. As temperature and time play a dominant role in residual strain formation, it can be found that the strain rate is 3 $\mu\varepsilon$/minutes at a cooling rate of 0.3°C/minutes.

The fifth phase corresponded to the fall of temperature from 88°C to 23°C at a cooling rate of 0.7°C/minutes when the high-low temperature oven door is opened. The strain curve decline followed the temperature curves as in the fourth phase. It can be observed that the residual compressive strain is 780 $\mu\varepsilon$ at the end of this phase. The relative difference between the residual strains obtained by the FBGSS and theoretical calculation is−7.8%, which means the variation in the residual strain can be monitor by the FBGSS in real time. Although the strain curves became flat when the temperature tends to room temperature, the strain rate is 7 $\mu\varepsilon$/minutes, which is much faster than that in the fourth phase mostly due to a faster cooling rate. When the

Table 5: Dynamic characteristics of the HSTs from the modal analysis module.

Characteristics	Steel–CFRP–steel	Steel	Relative difference (%)
Natural frequency (Hz)	1883	1974	−4.6
Damping ratio (%)	0.96	0.14	586
Weight (kg)	2.38	2.83	−15.9

temperature is equal to room temperature, the hybrid HST with sandwich walls is created.

According to the above analysis, the residual strains of the CFRP layers in sandwich walls transform from tensile strains to compressive strains during the dwell stage, and the total residual compressive strain is 810 $\mu\varepsilon$ throughout the cooling phase Table 4 compares the longitudinal residual strains of the fiber layers in hybrid metal–composite structures with different material combinations in the recently published literature. It can be observed that the residual strain values measured in this study are in the same order of magnitude as those in the literature, and the specific values are determined by the material combination, stacking sequence, and curing process [34]. Both low co-cure temperature and a small cooling rate can decrease the residual compressive strains. However, they are time-consuming and inevitably increase the cost of the co-curing bonding product. Consequently, a compromise between these two factors must be found.

3.3. The Dynamic Characteristics of the HST. Acceleration FRFs of 7 excitation points for the HSTs with both steel–CFRP–steel sandwich walls and steel walls are processed by the LMS analysis system as shown in Figure 10. Dynamic characteristics of the HSTs from the modal analysis module are given in Table 5. It is observed that the damping of the HST with both steel–CFRP–steel sandwich walls is 586% higher than that of the HST with steel walls. The extra increase comes from the intrinsic properties of CFRP layers, such as high specific stiffness and good damping capacity. However, the HST with steel–CFRP–steel sandwich walls has a lower first natural frequency (4.6% reduction) and mass (15.9% weight reduction). The embedded FBGSS measures strain response by the FBG interrogator simultaneously, and frequency spectra can be obtained from postprocessing with fast Fourier transformation. However, it failed to obtain the natural frequency because of the slight strain response.

4. Conclusion

This study presents a novel hybrid HST with sandwich walls based on steel skins and a unidirectional CFRP composite core and a detailed fabrication method with embedded FBG sensors. The encapsulated FBGTS and bare FBGSS are combined to monitor the temperature and strain history. The following conclusions can be drawn from the results obtained:

(a) Fabrication method of the hybrid HST with metal–FRP–metal sandwich walls is feasible. Through the embedded FBG sensors, the process temperatures and the variation of the residual strain can obtain in real time. It verifies that the sandwich walls can integrate with sensors to the hybrid metal–composite structure, which has potential application for machine tools structures.

(b) Dynamic characteristics of the hybrid HST and the steel HST are tested. The damping of the hybrid HST is 586% higher than that of the steel HST, while the hybrid HST has a lower first natural frequency (4.6% reduction) and mass (15.9% weight reduction).

(c) The hybrid HST with metal–FRP–metal sandwich walls has undergone complex residual strains history during the whole fabrication process. In the dwell stage, there are tensile strains, and the maximal value is 45 $\mu\varepsilon$. In the cooling stage, the tensile strains transform into compressive strains because of the mismatch of the CTE of the steel plates and the CFRP layers. In addition, the strain rate is about 10 times of cooling rate, and that strain rate is 3 $\mu\varepsilon$/minutes at a cooling rate of 0.3°C/minutes and 7 $\mu\varepsilon$/minutes at a cooling rate of 0.7°C/minutes, respectively. As most residual strains are directly related to the difference between the co-cure temperature and room temperature, both a low co-cure temperature and a slow cooling rate can decrease the residual compressive strains. Both co-cure temperature and cooling rate can profoundly affect the size and state of the residual strains, which are critical to product performance.

(d) Due to the monitoring capacity of the internal state, the embedded FBG sensors can also be used for online health monitoring and safety evaluation to build intelligent machine tools structures.

Data Availability

All data experiments can be found in the manuscript.

Conflicts of Interest

The authors declare that they have no conflicts of interest.

Acknowledgments

The project was supported by Wuhan University of Technology and Wuhan Textile University.

References

[1] F. Meo, A. Merlo, M. Rodriguez et al., "Advanced hybrid mechatronic materials for ultra precise and high performance machining systems design," in *Innovative Production Machines and Systems: Fourth I*PROMS Virtual International Conference*, Cardiff University, UK, 2008.

[2] F. Aggogeri, A. Borboni, A. Merlo, N. Pellegrini, and R. Ricatto, "Vibration damping analysis of lightweight structures in machine tools," *Materials*, vol. 10, no. 3, pp. 1–15, 2017.

[3] S. P. Mai, "Experiment on box-section sandwich beams in three-point bending," *Journal of Sandwich Structures & Materials*, vol. 16, no. 5, pp. 534–550, 2014.

[4] L. C. Hollaway, "A review of the present and future utilisation of FRP composites in the civil infrastructure with reference to their important in-service properties," *Construction and Building Materials*, vol. 24, no. 12, pp. 2419–2445, 2010.

[5] H. S. Kim, S. W. Park, and D. G. Lee, "Smart cure cycle with cooling and reheating for co-cure bonded steel/carbon epoxy composite hybrid structures for reducing thermal residual stress," *Composites Part A: Applied Science and Manufacturing*, vol. 37, no. 10, pp. 1708–1721, 2006.

[6] G. Zhu, G. Sun, Q. Liu, G. Li, and Q. Li, "On crushing characteristics of different configurations of metal-composites hybrid tubes," *Composite Structures*, vol. 175, pp. 58–69, 2017.

[7] G. Sun, Z. Wang, H. Yu, Z. Gong, and Q. Li, "Experimental and numerical investigation into the crashworthiness of metal-foam-composite hybrid structures," *Composite Structures*, vol. 209, pp. 535–547, 2019.

[8] P. P. Parlevliet, H. E. N. Bersee, and A. Beukers, "Residual stresses in thermoplastic composites—a study of the literature. Part III: effects of thermal residual stresses," *Composites Part A: Applied Science and Manufacturing*, vol. 38, no. 6, pp. 1581–1596, 2007.

[9] R. Prussak, D. Stefaniak, E. Kappel, C. Hühne, and M. Sinapius, "Smart cure cycles for fiber metal laminates using embedded fiber Bragg grating sensors," *Composite Structures*, vol. 213, pp. 252–260, 2019.

[10] S. Ghiasvand, A. Airoldi, P. Bettini, and C. Mirani, "Analysis of residual stresses and interface damage propagation in hybrid composite/metallic elements monitored through optical fiber sensors," *Aerospace Science and Technology*, vol. 129, p. 107373, 2022.

[11] J. J. Homan, "Fatigue initiation in fibre metal laminates," *International Journal of Fatigue*, vol. 28, no. 4, pp. 366–374, 2006.

[12] S. U. Khan, R. C. Alderliesten, and R. Benedictus, "Post-stretching induced stress redistribution in fibre metal laminates for increased fatigue crack growth resistance," *Composites Science and Technology*, vol. 69, no. 3–4, pp. 396–405, 2009.

[13] A. R. Ghasemi and M. M. Mohammadi, "Residual stress measurement of fiber metal laminates using incremental hole- drilling technique in consideration of the integral method," *International Journal of Mechanical Sciences*, vol. 114, pp. 246–256, 2016.

[14] P. Hofslagare, "Residual stress measurement on fibre-metal-laminates," *Journal of Neutron Research*, vol. 11, no. 4, pp. 215–220, 2003.

[15] J. Wiedemann, R. Prussak, E. Kappel, and C. Hühne, "In-situ quantification of manufacturing-induced strains in fiber metal laminates with strain gages," *Composite Structures*, vol. 297, article 115967, 2022.

[16] S. Tinkloh, T. Wu, T. Tröster, and T. Niendorf, "A micromechanical-based finite element simulation of process-induced residual stresses in metal–CFRP–hybrid structures," *Composite Structures*, vol. 238, article 111926, 2020.

[17] J. Xue, W. X. Wang, Y. Takao, and T. Matsubara, "Reduction of thermal residual stress in carbon fiber aluminum laminates using a thermal expansion clamp," *Composites Part A: Applied Science and Manufacturing*, vol. 42, no. 8, pp. 986–992, 2011.

[18] T. Wu, S. Degener, S. Tinkloh et al., "Characterization of residual stresses in fiber metal laminate interfaces—a combined approach applying hole-drilling method and energy-dispersive X-ray diffraction," *Composite Structures*, vol. 299, article 116071, 2022.

[19] P. P. Parlevliet, H. E. N. Bersee, and A. Beukers, "Residual stresses in thermoplastic composites—a study of the literature—part II: experimental techniques," *Composites Part A: Applied Science and Manufacturing*, vol. 38, no. 3, pp. 651–665, 2007.

[20] X. Geng, M. Jiang, L. Gao et al., "Sensing characteristics of FBG sensor embedded in CFRP laminate," *Measurement*, vol. 98, pp. 199–204, 2017.

[21] M. Mulle, H. Wafai, A. Yudhanto et al., "Process monitoring of glass reinforced polypropylene laminates using fiber Bragg gratings," *Composites Science and Technology*, vol. 123, pp. 143–150, 2016.

[22] M. Mulle, F. Collombet, P. Olivier, and Y. H. Grunevald, "Assessment of cure residual strains through the thickness of carbon-epoxy laminates using FBGs, part I: elementary specimen," *Composites Part A: Applied Science and Manufacturing*, vol. 40, no. 1, pp. 94–104, 2009.

[23] H. K. Kang, D. H. Kang, H. J. Bang, C. S. Hong, and C. G. Kim, "Cure monitoring of composite laminates using fiber optic sensors," *Smart Materials and Structures*, vol. 11, no. 2, pp. 279–287, 2002.

[24] Q. Wang, L. Gao, X. Wang et al., "Numerical analysis and fiber Bragg grating monitoring of thermocuring processes of carbon fiber/epoxy laminates," *Polymer Testing*, vol. 62, pp. 287–294, 2017.

[25] R. Prussak, D. Stefaniak, C. Hühne, and M. Sinapius, "Evaluation of residual stress development in FRP-metal hybrids using fiber Bragg grating sensors," *Production Engineering*, vol. 12, no. 2, pp. 259–267, 2018.

[26] K. S. C. Kuang, L. Zhang, W. J. Cantwell, and I. Bennion, "Process monitoring of aluminum-foam sandwich structures based on thermoplastic fibre-metal laminates using fibre Bragg gratings," *Composites Science and Technology*, vol. 65, no. 3–4, pp. 669–676, 2005.

[27] K. O. Hill and G. Meltz, "Fiber Bragg grating technology fundamentals and overview," *Journal of Lightwave Technology*, vol. 15, no. 8, pp. 1263–1276, 1997.

[28] M. Majumder, T. K. Gangopadhyay, A. K. Chakraborty, K. Dasgupta, and D. K. Bhattacharya, "Fibre Bragg gratings in structural health monitoring—present status and applications," *Sensors and Actuators A: Physical*, vol. 147, no. 1, pp. 150–164, 2008.

[29] ASTM A 29/A 29M-05, Standard Specification for Steel Bars, Carbon and Alloy, Hot-Wrought, General Requirements for, ASTM Committee, 2005.

[30] D. W. Lee, B. J. Park, S. Y. Park, C. H. Choi, and J. I. Song, "Fabrication of high-stiffness fiber-metal laminates and study of their behavior under low-velocity impact loadings," *Composite Structures*, vol. 189, pp. 61–69, 2018.

[31] M. Harhash, O. Sokolova, A. Carradó, and H. Palkowski, "Mechanical properties and forming behaviour of laminated

steel/polymer sandwich systems with local inlays - Part 1," *Composite Structures*, vol. 118, pp. 112–120, 2014.

[32] R. F. Gibson, *Principles of Composite Material Mechanics*, Taylor & Francis Group, 4th edition edition, 2016.

[33] Y. Xu, H. Li, Y. Yang, Y. Hu, and J. Tao, "Determination of residual stresses in Ti/CFRP laminates after preparation using multiple methods," *Composite Structures*, vol. 210, pp. 715–723, 2019.

[34] P. P. Parlevliet, H. E. N. Bersee, and A. Beukers, "Residual stresses in thermoplastic composites—a study of the literature–Part I: formation of residual stresses," *Composites Part A: Applied Science and Manufacturing*, vol. 37, no. 11, pp. 1847–1857, 2006.